Dynamics of Taylor bubble under chemical reaction enhanced mass transfer in minichannel

Hao Cheng, Dominique Tarlet, Lingai Luo, Yilin Fan

▶ **To cite this version:**

Hao Cheng, Dominique Tarlet, Lingai Luo, Yilin Fan. Dynamics of Taylor bubble under chemical reaction enhanced mass transfer in minichannel. Separation and Purification Technology, 2024, 341, pp.126900. 10.1016/j.seppur.2024.126900 . hal-04523552

HAL Id: hal-04523552
https://hal.science/hal-04523552

Submitted on 27 Mar 2024

HAL is a multi-disciplinary open access archive for the deposit and dissemination of scientific research documents, whether they are published or not. The documents may come from teaching and research institutions in France or abroad, or from public or private research centers.

L'archive ouverte pluridisciplinaire **HAL**, est destinée au dépôt et à la diffusion de documents scientifiques de niveau recherche, publiés ou non, émanant des établissements d'enseignement et de recherche français ou étrangers, des laboratoires publics ou privés.

Dynamics of Taylor bubble under chemical reaction enhanced mass transfer in minichannel

Hao CHENG, Dominique TARLET, Lingai LUO, Yilin FAN*

Nantes Université, CNRS, Laboratoire de Thermique et énergie de Nantes, LTeN, UMR6607, 44000, Nantes, France

Abstract:

Taylor bubble dynamic characteristics of CO_2 chemical absorption into MEA aqueous solution in a vertical minichannel were systematically investigated in this study. The generation, movement, and shrinkage of bubbles in the minichannel were visualized and monitored using a high-speed camera, and their dynamic behaviors were characterized by image analysis method. The effects of gas and liquid Re numbers and absorbent concentration on two-phase flow patterns, bubble generation frequency, initial bubble length, bubble length decrease rate, and bubble velocity were examined and analyzed. Results showed that chemical reaction-enhanced mass transfer hindered the bubble cap penetration into the main channel, and alleviated the bubble neck thinning, both effects inhibiting the bubble generation. A new Damköhler number (*Da*)-based correlation has been proposed to predict the initial Taylor bubble length, showing good prediction accuracy for experimental data in the literature using different absorbents. Results also showed that before the formation of sphere bubble at the end of absorption, an approximate linear relationship exists between bubble length decrease rate and bubble velocity, with the slop decided by chemical reaction rate that could be characterized by the *Da* number. Finally, a simple model has been developed to determine the effective channel length at a given operating condition, providing design guidelines for microchannel-based miniaturized CO_2 absorbers.

Keywords: Carbon capture, CO_2 chemical absorption, microchannel reactor, gas-liquid two-phase flow, Taylor bubble dynamics

* Corresponding author. E-mail address: yilin.fan@univ-nantes.fr (Y. Fan)

Nomenclature

C_{MEA}	MEA volumetric concentration (%)
D	Diffusion coefficient ($m^2.s^{-1}$)
d_h	Hydraulic diameter (m)
k_L	Physical mass transfer coefficient ($m.s^{-1}$)
k_{ov}	Overall reaction rate (s^{-1})
l_t	Bubble length at time t (m)
l_0	Initial bubble length (m)
L	Channel length (m)
L_e	Effective channel length (m)
L_e^*	Dimensionless effective channel length
Q	Volumetric flow rate ($ml.h^{-1}$)
T	Experimental temperature (K)
t	Bubble moving time (s)
v	Bubble velocity ($m.s^{-1}$)
U	Superficial velocity ($m.s^{-1}$)
w	Main channel width (m)
y	Bubble cap pixel position

Dimensionless number

Ca	Capillary number, $Ca = \mu U/\sigma$
Da	Damköhler number, $Da = k_{ov} \cdot {d_h}^2/D$
Re	Reynolds number, $Re = \rho U d_h/\mu$
Re_{TP}	Two-phase flow Reynolds number, $Re_{TP} = \rho_L(U_G + U_L)d_h/\mu_L$
Ha	Hatta number, $Ha = \sqrt{D{k_{ov}/k_L}^2}$

Greek symbols

δ_{neck}	Bubble neck thickness (m)
μ	Dynamic viscosity ($Pa.s$)
σ	Surface tension ($N.m^{-1}$)
$\boldsymbol{\rho}$	Density ($kg.m^{-3}$)
$\boldsymbol{\Delta}$	Difference
f	Bubble generation frequency (s^{-1})
$\emptyset$	Relative uncertainties
τ_b	Slug bubble generation duration (s)
γ	Gas-liquid inlet angle
∂	Pixel calibration scale (μm)

Subscripts

b	Bubble
c	Channel
G	Gas
L	Liquid
f	Front cap
r	Rear cap
TP	Two-phase flow
0	Initial status

1

Introduction

The quest for process intensification through device miniaturization has stimulated the rapid development and application of microfluidic-based technologies in many industrial sectors [1–3]. Facing the carbon neutrality target by 2050 [4], one current research hot spot in this area is the use of miniaturized absorbers/reactors for CO_2 capture through chemical absorption [5,6]. Instead of using traditional large-scale absorption equipment, the gas phase (CO_2) and liquid phase (chemical solvent) come into contact and flow in a channel with characteristic size in micro or millimeter, offering numerous advantages compared to its counterpart such as enhanced mass transfer, smaller occupied space, safer operation and improved energy recovery efficiency [7,8].

Depending on operating conditions, gas-liquid two-phase flow could exhibit different flow patterns in micro/millichannel, commonly including bubbly flow, slug flow, slug annular flow and churn flow [9–11]. Among them, the slug (Taylor) flow pattern shows better stability, controllability and more uniform dispersity, therefore attracting more attention and interest from researchers. A single (CO_2) Taylor bubble may undergo several stages in the microchannel due to chemical reaction, from bubble generation, bubble moving and shrinkage till its vanishing (totally absorbed into the liquid phase). Since the two-phase mass transfer is closely related to the bubble hydrodynamic behaviors [12–14], fully understanding the chemical reaction accompanied Taylor bubble dynamics becomes essential to characterize and improve the absorption efficiency of microchannel-based CO_2 absorbers.

Many researches have been focused on the bubble generation process through T-junction microchannel and the breakup mechanism [15,16]. For example, Fu et al. [17] experimentally investigated the bubble generation mechanism of $N_2 - H_2O$/glycerol system in a 120 μm×40 μm T-type microchannel, showing that the effect of gas-liquid-solid three-phase squeezing contributed to stable and uniform bubble breakup. Higher gas and liquid flow rates could accelerate the bubble neck thinning, therefore favoring the pinch-off. van Steijn et al. [18] experimentally verified that the tip structure at the main channel would cause a reversal liquid flow which promoted the neck collapse. Yao et al. [19] and Sheng et al. [20] both showed that increasing the liquid phase viscosity could stabilize and promote the bubble generation. Garstecki et al. [21] reported that at small capillary number (Ca<10^{-2}) the bubble break-up is dominated by gas-liquid-solid three-phase squeezing on the gas neck. A linear model that relates the initial bubble length (l_0) and the ratio of gas and liquid flow rates has been proposed

($\frac{l_0}{w} = a + b\frac{Q_G}{Q_L}$), with w being the channel width and a, b the fitting constants for different gas-liquid manipulation ranges and microchannel geometries. Since then, other improved prediction models have been proposed for more complex situations, taking influences of structure and two-phase physical properties into account [19,22–24]. However, most of these models (cf. Table 3 of this paper) were developed for two-phase flow system with little or low mass transfer, thus could not fit the situation of CO_2 chemical absorption in micro/minichannel. Relatively fewer studies have been devoted to investigate the Taylor bubble generation under chemical reaction enhanced mass transfer despite more complicated breakup mechanisms [11,12]. Zhu et al. [24] experimentally investigated CO_2 chemical absorption into aqueous solution in microchannel and reported the inhibitory effect of chemical reaction on the formed bubble length. Such effect has also been observed by Ma et al. [25] and Yin et al. [26], but the underlying inhibition mechanism requires further elucidation. Noteworthy is the l_0 prediction correlation proposed by Yin et al. [26], to the best of authors' knowledge, the only one in the literature that includes a chemical reaction related parameter, the Hatta number (*Ha*), to indicate the impact of chemical reaction. However, the calculation of *Ha* is not straightforward. Besides the physio-chemical properties of the two-phase flow system, the bubble generation duration needs to be known by experimental measurement, resulting in complicated, laborious, and sometimes inaccurate estimation. An easy-to-use, more accurate and general prediction correlation is still in need for bubble generation process in microchannel under chemical reaction accompanied mass transfer.

Once generated, the (CO_2) bubble moves along with the liquid phase in the main channel, and its volume shrinks due to the two-phase mass transfer. Compared to physical diffusion-dominated mass transfer, the chemical reaction-enhanced mass transfer would significantly alter bubble moving dynamics in the microchannel [12,27]. The mass transfer rate for a single Taylor bubble becomes unsteady but shows a downward trend due to the varied concentration gradient in the liquid phase [28,29], evidenced by the decreased shrinkage of bubble volume/length over moving time. CO_2 bubble velocity (v_b) also shows a more complex trend and differs from the two-phase superficial velocity (U_{TP}) which is the case under physical diffusion-dominated mass transfer. The experimental results of Zhou et al. [12] clearly showed that v_b decreased more rapidly with the increasing concentration of aqueous MEA solution (C_{MEA}). To further reveal the distinguished characteristics of bubble dynamics under chemical reaction-enhanced mass transfer, Yin et al. [30] related the bubble length reduction rate ($\Delta l/l_0$) with v_b by an empirical model: $v_b/U_{TP} = 1.29(1 - \Delta l/l_0)$. However, the proposed

correlation is only based on physical parameters. The possible significant impact of chemical reaction on the transient bubble velocity and bubble length change may need further clarification.

The above literature review highlights that the basic understanding of Taylor bubble dynamics in micro/minichannel under chemical reaction-enhanced mass transfer is still insufficient. At bubble generation stage, it has been reported that the accelerated gas absorption at the gas-liquid interface could inhibit the bubble generation. But the inhibitory effect on different bubble generation stages, especially on bubble neck shrinkage and pinch-off, has not yet been elaborated in detail. The enhanced mass transfer process due to the chemical reaction also shortens l_0. However, the majority of prediction correlations fail to reflect the effect of chemical reaction on l_0 of CO_2 bubble, while a simple but more general model is still in need. At bubble moving stage, it is shown that the intensified mass transfer would promote the bubble shrinkage, resulting in the varied v_b. Nevertheless, the relation between them is still not enough clear, especially regarding the impact of absorbent concentrations. Moreover, insights are still lacking regarding the effective use of the microchannel length at a given operating condition, which is a key design parameter for microchannel-based CO_2 absorbers.

The aim of this work is to fill the above-mentioned research gaps by systematically investigating and characterizing the effects of chemical reaction accompanied mass transfer on Taylor bubble dynamics in micro/minichannel. For this purpose, CO_2 absorption experiments by MEA solution (C_{MEA}=1%, 3%, 5% and 10%) were performed in a T-type straight minichannel (1.5 mm × 1.5 mm × 80 mm) under different gas and liquid flow rates ($Q_{G:}$ 30-180 ml/h; $Q_{L:}$ 10-50 ml/h). The evolution of CO_2 bubble shape during its generation and its shrinkage was visualized and monitored by a high-speed camera, and its dynamic behaviors were characterized by image processing. Effect of gas and liquid flow rates and absorbent concentration on two-phase flow pattern, bubble generation frequency (f_b), bubble initial length (l_0) and length decrease rate ($\Delta l_t/\Delta t$), and bubble velocity (v_b) were examined and analyzed. Based on the obtained results, new correlations were proposed to better predict these Taylor bubble dynamic parameters under chemical reaction accompanied mass transfer in minichannel. Furthermore, an empirical model has been proposed to estimate the effective length of the microchannel at a given operating condition, offering an engineering-oriented design guideline for microchannel-based CO_2 absorbers. These findings may contribute to gain new insights into underlying mechanisms of bubble dynamics, and to the design and optimization of highly efficient microchannel-based CO_2 absorbers for carbon capture in industrial processes.

2. Materials and methods

2.1 Experimental setup

Figure 1 shows a schematic view of the experimental setup for optical measurement as well as the microchannel CO_2 absorber tested in this study. CO_2 (Air Liquide, 99.9% purity) was used as the gas phase, being fed to the minichannel absorber by a gas mass flow controller (Brooks SLA 5850, calibrated with CO_2). Aqueous Monoethanolamine (MEA) solution (Arcane-industries, France, purity ≥ 99%) with different concentrations (C_{MEA}=1%, 3%, 5% and 10% vol.) was used as the liquid phase, its flowrate being controlled by a micro syringe pump (kdScientific-267, USA). The minichannel was vertically positioned, CO_2 and MEA solution were injected to the bottom-inlets and the product was collected from the top-outlet. A high-speed camera (FASTCAM 1080K-M4 SA-X2) with 12× lens (LaVision VZ10-0518) was used to monitor and record bubble generation and shape variation in the minichannel at 2000 fps. A 36w flat uniform cold light source (LEDVANCE, 600mm×600mm, 4000K) was positioned behind the minichannel absorber to provide background illumination during images recording. The measuring range and precision of these instruments are given in Table 2.

The minichannel CO_2 absorber has a square cross-section of 1.5 mm×1.5 mm, and a straight channel of 80 mm in length. It has a T-type junction for the contact of gas and liquid phases, with two inlet branches having the same dimensions of 1.5 mm in width, 1.5 mm in height and 10 mm in length (cf. Fig. 1b). The structure of minichannel absorber was grooved by digital carving on the surface of a polymethyl methacrylate (PMMA) cuboid with dimensions of 115 mm in length, 30 mm in width and 20 mm in height. Another PMMA cuboid was prepared with grooves filled with rubber strips around the T-junction and the main straight channel to prevent the leakage. Note that an opaque sheet was inserted between two PMMA pieces to reduce the light reflection during image capturing (cf. Fig. 1c). Bolts were used for further sealing.

The tested flow rate range was 30-180 ml/h for gas phase and 10-50 ml/h for liquid phase, respectively. The corresponding Reynolds number range was 0.63-3.78 for Re_G and 1.89-9.45 for Re_L, respectively. Note that the Reynolds number ($Re = \rho U d_h/\mu$) was calculated based on the superficial velocity (U) of gas or liquid and the hydraulic diameter of the minichannel (d_h=1.5 mm). All experiments were conducted under 293 K and atmospheric pressure. For each measurement, it took about 5 minutes for two-phase flow to stabilize. Good stability and reproducibility of two-phase flow pattern and bubble dynamic behaviors have been observed within the tested flow rate ranges.

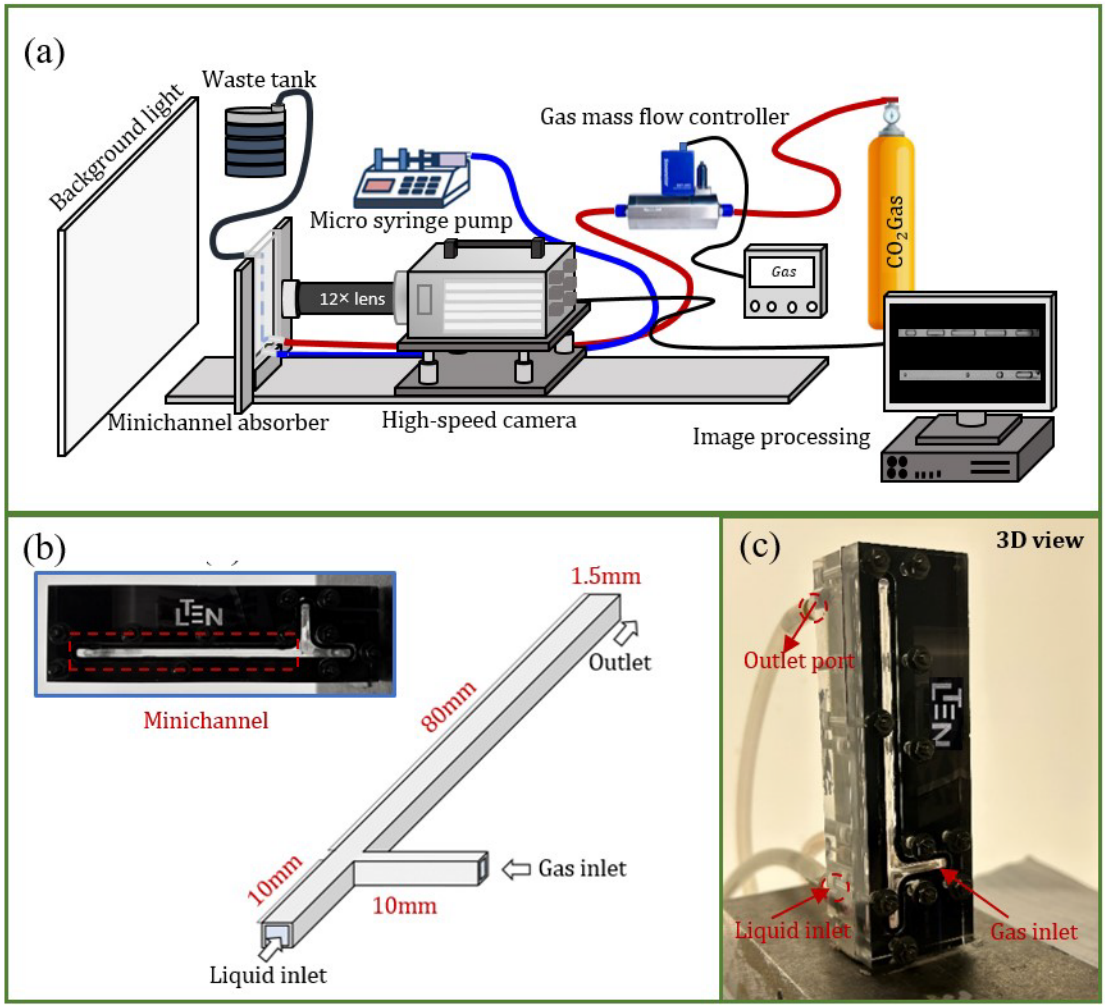

Figure 1. Experimental setup and device. (a) Schematic diagram of the test-rig; (b) Geometry and dimensions of the T-junction minichannel; (c) 3-D photo view of the CO_2 absorber prototype.

2.2 Chemical reaction theory

Chemical reaction rate directly affects the two-phase mass transfer and CO_2 absorption performance in the minichannel absorber. In this study, the primary amines-MEA was used as CO_2 absorbent owing to its quick reaction rate and high CO_2 selectivity. The chemical reaction between MEA aqueous solution and CO_2 can be summarized as zwitterion mechanism [31] consisting of two steps. In the first step, the quick reaction between MEA molecular and CO_2 forms the intermediate zwitterion (Eq. 1). In the second step, the intermediate zwitterion is quickly transformed to carbamate ion by losing a proton (Eq. 2):

$$CO_2 + R'NH_2 = R'NH_2{}^+COO^- \quad (1)$$

$$R'NH_2{}^+COO^- + R'NH_2 = R'NHCOO^- + R'NH_3{}^+ \quad (2)$$

where R′ is CH_2CH_2OH, $R'NH_2{}^+COO^-$ and $R'NHCOO^-$ represent the zwitterion and the carbamate ion, respectively. The whole reaction process between MEA aqueous solution and CO_2 can be expressed as Eq. 3.

$$CO_2 + 2CH_2CH_2OHNH_2 \rightleftharpoons CH_2CH_2OHNHCOO^- + CH_2CH_2OHNH_3{}^+ \quad (3)$$

This reaction is slightly exothermic, but the impact of reaction heat on CO_2 absorption performance and two-phase mass transfer process is negligible [32]. The solvent density (ρ_L), viscosity (μ_L), two-phase surface tension (σ), diffusion coefficient (D) and overall chemical reaction rate (k_{ov}) of CO_2 − MEA aqueous solution reaction system are referred to references [30,33] and summarized in Table 1.

Table 1. Physicochemical properties of CO_2-MEA aqueous solution reaction system

C_{MEA}	Density $\rho_L(\mathrm{kg/m^3})$	Viscosity $\mu_L \times 10^3(\mathrm{Pa.s})$	Diffusivity $D \times 10^9(\mathrm{m^2/s})$	Surface tension $\sigma \times 10^3(\mathrm{N/m})$	Chemical reaction rate $k_{ov}(\mathrm{s^{-1}})$
1%	998.6	0.978	1.99	38.56	451.06
3%	998.9	0.986	2.03	38.35	1403.18
5%	999.1	1.041	2.08	38.24	2355.24
10%	1004.2	1.098	2.15	38.09	4510.31

2.3 Determination of bubble length and velocity

For a detailed analysis of CO_2 bubble dynamics under chemical reaction, a high-speed camera was used to capture the two-phase flow behaviors in minichannel. Bubble dynamic parameters were obtained by processing two-phase flow images captured by high-speed camera, using MATLAB (v2020a) based image analysis method [34]. The image processing procedure is explained in Fig. 2 and described as below.

Firstly, the grayscale image of two-phase flow in the minichannel absorber was prepared (step 1). Then, the gas-liquid interface was detected by using edge recognition algorithm 'Sobel'. The recognized bubble area (blue part) and its frontier (red dash line) were further compared with those in the original image so as to improve the boundary recognition accuracy (step 2). After that, the grayscale image was converted into a binary image using 'imbinarize' algorithm for the purpose of detecting the pixel positions of a single bubble front & rear bubble caps in the minichannel (step 3). By calibrating the actual size represented by each pixel, the bubble dynamic parameters could finally be calculated (step 4).

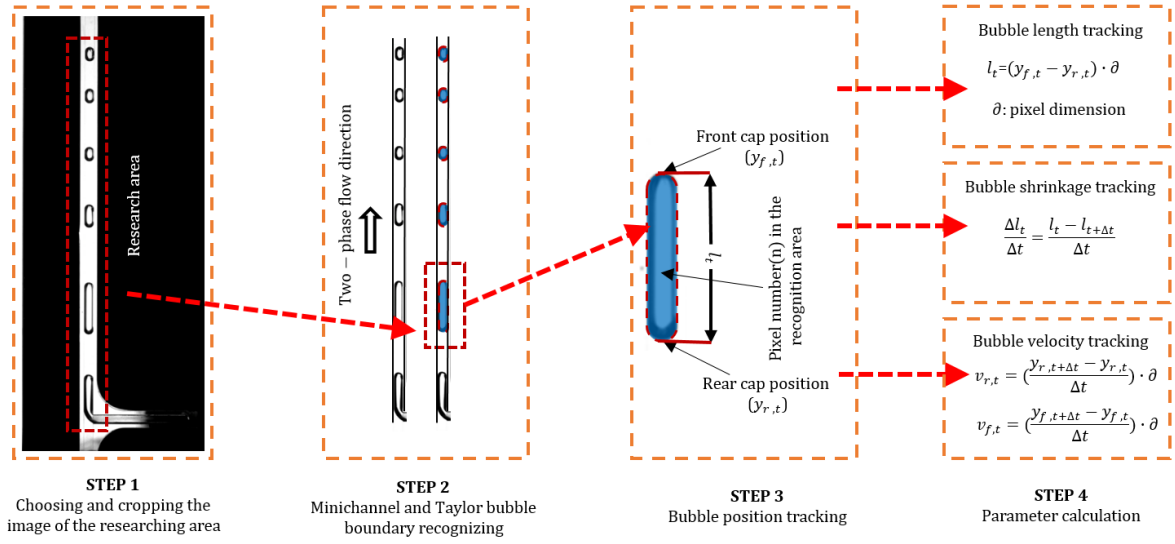

Figure 2. MATLAB based image processing method for calculating bubble dynamic parameters.

To reduce the impact of two-phase flow instability on the generation of CO_2 bubbles in the minichannel, the average initial CO_2 bubble length (l_0) generated within 20 s was calculated for each gas-liquid manipulation condition. The instantaneous bubble length (l_t) from bubble generation to disappearance was obtained by the image processing method described above, calculated as:

$$l_t = (y_{f,t} - y_{r,t}) \times \partial \tag{4}$$

where $y_{f,t}$ and $y_{r,t}$ are front and rear bubble cap pixel position at time t, respectively. ∂ is the calibration size of 1 pixel (18.75 μm). The initial bubble generated time was set as the initial time ($t = 0$). The transient bubble length decrease rate ($\Delta l_t/\Delta t$) was calculated by Eq. 5 with Δt equaling to 0.1 s:

$$\frac{\Delta l_t}{\Delta t} = \frac{l_t - l_{t+\Delta t}}{\Delta t} \tag{5}$$

The bubble velocity (v_b) at time t is calculated as the average of the front bubble cap velocity ($v_{f,t}$) and rear bubble cap velocity ($v_{r,t}$), shown in Eqs. 6-8.

$$v_{f,t} = \frac{(y_{f,t+\Delta t} - y_{f,t}) \times \partial}{\Delta t} \tag{6}$$

$$v_{r,t} = \frac{(y_{r,t+\Delta t} - y_{r,t}) \times \partial}{\Delta t} \tag{7}$$

$$v_b = \frac{v_{f,t} + v_{r,t}}{2} \tag{8}$$

2.4 Uncertainty Analysis

An estimation on the uncertainties of experimentally measured parameters and calculated results was performed, as listed in Table 2. CO_2 mass flow controller (Brooks SLA 5850) and syringe pump (kdScientific-267) were calibrated by standard volumetric method [35] and relative uncertainties were estimated to be ± 0.03 ml/min and ± 0.1 ml/h, respectively. The experimental temperature is measured by calibrated K-type thermocouple (± 0.5 K). The uncertainties of calculated parameters were estimated based on error propagation method [36]. In this study, bubble shape parameters were captured by high-speed camera (FASTCAM 1080K-M4 SA-X2) and the largest uncertainty was estimated to be 2 pixels (37.5 μm).

Under the testing range of this study, the maximum relative uncertainty of l_0 is estimated to be $\pm 1.67\%$. Bubble neck thickness (δ_{neck}) is captured with the $12\times$ lens and the maximum relative uncertainty is estimated to be $\pm 0.85\%$. The measured v_b is larger than 2.8 mm/s and the maximum relative uncertainty is estimated to be $\pm 11.7\%$.

Table 2. Estimated uncertainties of measured and calculated parameters

Measured parameters	Symbol	Unit	Measuring range	Measuring precision
Liquid volumetric flow rate	Q_L	ml/h	0-400	±0.1
Gas volumetric flow rate	Q_G	ml/min	0-3.0	±0.03
High-speed camera pixels	-	μm/pixel	-	2 pixels (±37.5 μm)
Experimental temperature	T	K		±0.5
Calculated parameters			**Maximum relative uncertainties Ø**	
Initial bubble length	l_0	mm	±1.67%	
Bubble neck thickness	δ_{neck}	mm	±0.85%	
Bubble length decrease rate	$\Delta l_t/\Delta t$	mm/s	±9.37%	
Bubble velocity	v_b	mm/s	±11.7%	
Microchannel effective length	L_e	mm	±0.7%	

3. Results and discussion

3.1 Two-phase flow pattern

Two-phase flow pattern indicates the shape and spatial distribution of CO_2 bubbles and MEA liquid slugs in the minichannel, reflecting also their hydrodynamic and mass transfer characteristics [37]. Due to chemical reaction-accompanied mass transfer, the CO_2 − MEA two-phase flow system in minichannel shows quick unit bubble shrinkage and flow pattern transition. Three types of two-phase flow pattern were captured under the tested flow rate range (Q_L: 10-50 ml/h, Q_G: 30-180 ml/h) and MEA concentrations (C_{MEA}=1%-10% vol.), including bubbly flow, slug-bubbly flow and slug flow. Figure 3 illustrates some examples captured in the experiments. Note that annular flow and churn flow patterns were not observed due to relatively small Re_L and Re_G ranges of the current study.

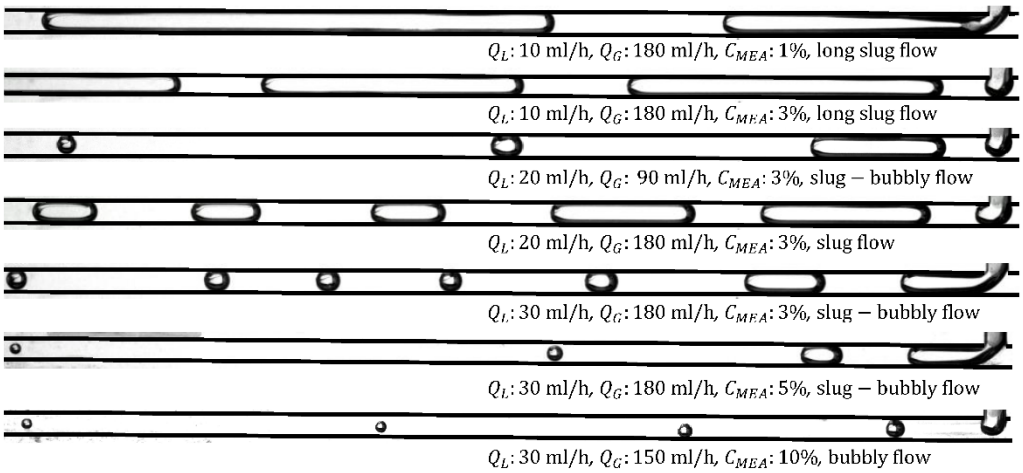

Figure 3. Typical CO_2/MEA aqueous solution two-phase flow patterns in minichannel captured in this study.

Figure 4 shows the effect of manipulation conditions on two-phase flow patterns and their transition. The increase of gas superficial velocity (U_G) leads to the increased bubble length, tending to form the slug flow pattern in minichannel. On the contrary, the increase of liquid superficial velocity (U_L) could enhance the renewal rate of absorbent around the CO_2 bubbles on one hand, and reduce the liquid-side mass transfer resistance on the other hand. Both effects intensify the mass transfer and promote the flow pattern transition from slug flow to slug-bubbly flow or bubbly flow. Furthermore, the higher C_{MEA} augments the reaction rate between CO_2 and MEA solution which accelerates the CO_2 absorption, bubbly flow and slug-bubbly flow being dominant on the flow map shown in Fig. 4d (C_{MEA}=10%).

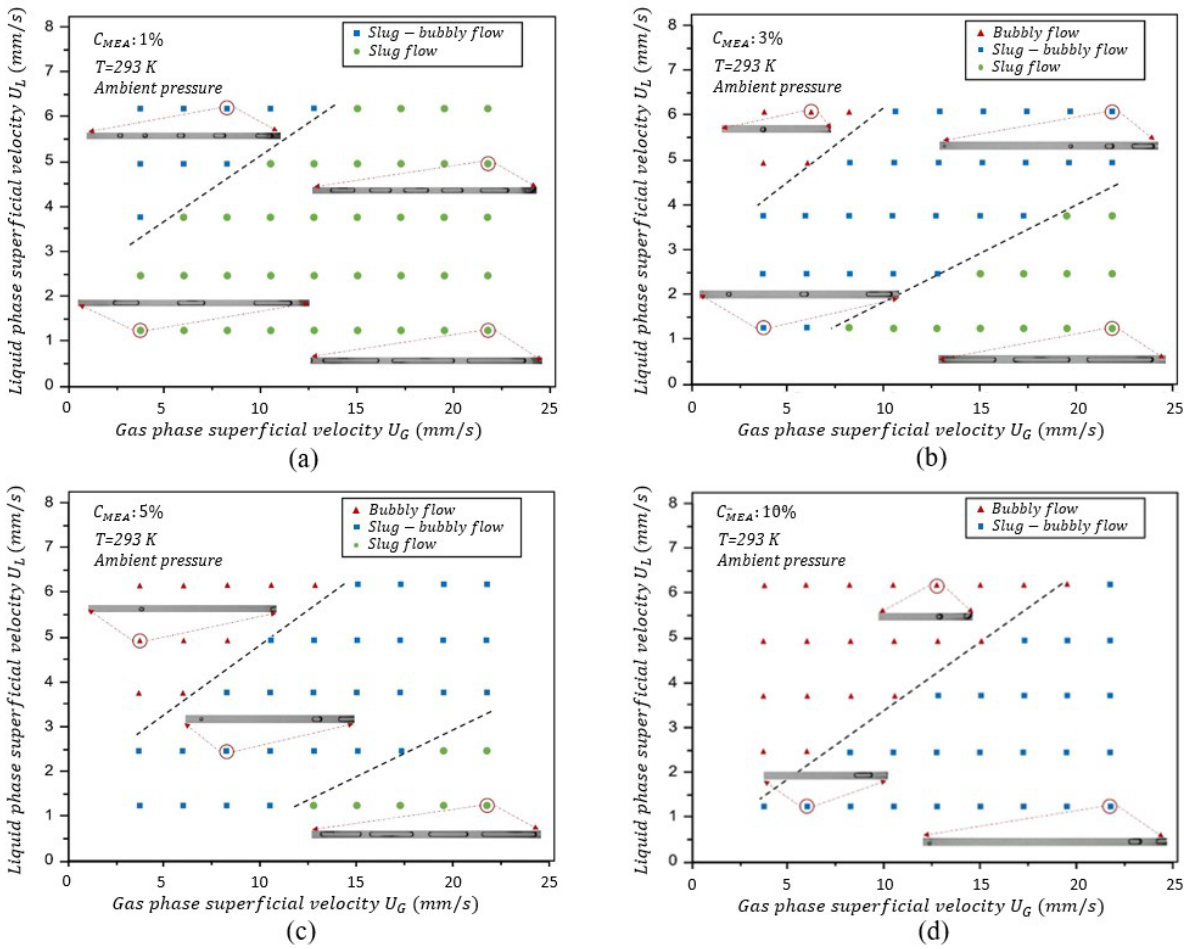

Figure 4. Two-phase flow map for CO_2 chemical absorption by MEA aqueous solution in minichannel. (a) $C_{MEA} = 1\%$; (b) $C_{MEA} = 3\%$; (c) $C_{MEA} = 5\%$; (d) $C_{MEA} = 10\%$. Conditions: Q_G=30-180 ml/h; Q_L=10-50 ml/h.

3.2 Bubble generation

The bubble generation process involves the injection of gas phase through the T-junction, its contact and interactions with the liquid phase till the pinch-off. In this sub-section, the chemical reaction-influenced bubble generation is discussed.

3.2.1 Bubble breakup mechanism

The bubble breakup mechanism is reported to be dependent on the Capillary number ($Ca = \mu_L U_L/\sigma$) [38,39] and the channel geometry [40]. For small Ca number condition such as in the current study ($3 \times 10^{-5} < Ca < 1.6 \times 10^{-4}$), the bubble generation at the T-junction mini/microchannel absorber can be attributed to the squeezing mechanism of gas-liquid-solid three phases [17]. It undergoes three stages, namely penetration, main channel axial expansion and pinch-off, as shown in Fig. 5. In penetration stage, the gas phase is forced into the main

channel by the mass flow controller to form the bubble cap and fill the T-junction section [41,42]. Then during the axial expansion stage, generated bubble cap is deformed by the pressure force of the liquid phase in contact and quickly extends in the main channel due to the continuous gas supply. In the meantime, the accumulated upstream pressure squeezes the bubble neck and reduces the bubble neck thickness (δ_{neck}). The pinch-off stage starts when the decrease of δ_{neck} accelerates, usually comes when $\delta_{neck} \leq 1/3d_h$. Once the accumulated shear force becomes greater than the surface tension [43], the bubble neck collapses and the gas bubble is formed.

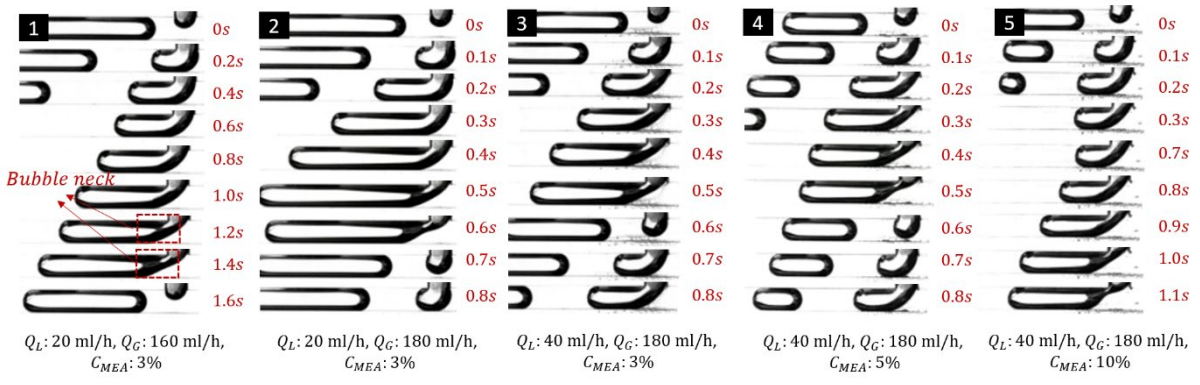

Figure 5. CO_2 bubble formation process in T-junction minichannel at different gas & liquid flow rates and MEA solution concentrations.

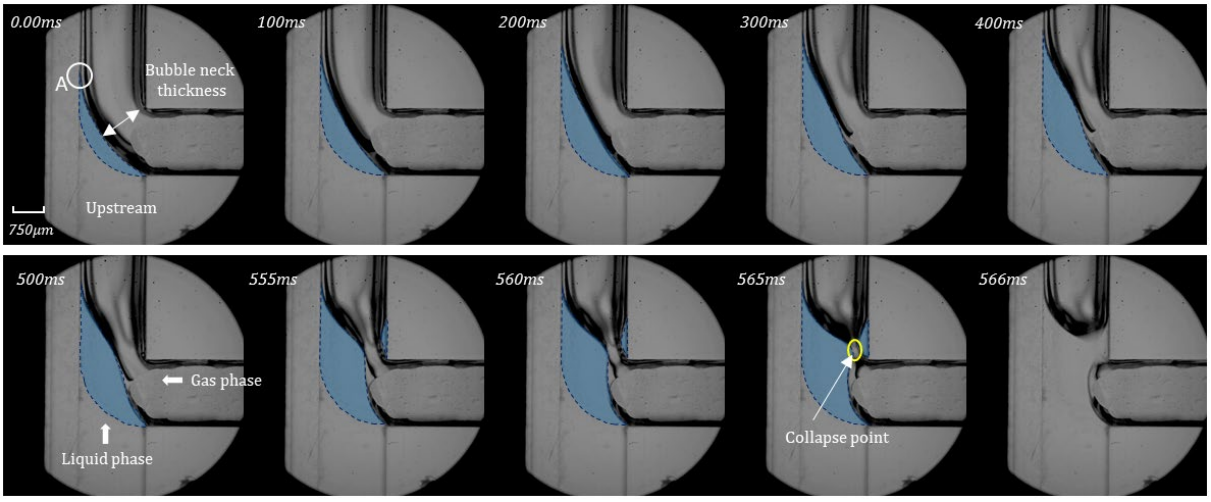

Figure 6. Bubble local neck collapse process captured by high-speed camera with 12× lens. Condition: C_{MEA}: 10%; Q_G: 180 ml/h; Q_L: 30 ml/h.

Figure 6 shows more details about the local bubble neck thinning (C_{MEA}: 10%, Q_G: 180 ml/h, Q_L: 30 ml/h). With the accumulation of liquid phase shear stress, the gas-liquid-solid three

phase contact point ('A' in Fig. 6) firstly moves downward and then stays almost immovable. In the meantime, the gas-liquid interface distorts and the neck thickness decreases. Finally, the squeezing of surrounding liquid results in the bubble neck collapse.

Figure 7 presents measured values of δ_{neck} under different Q_L, Q_G, and C_{MEA} conditions. At a given C_{MEA}, δ_{neck} decreases faster with the increase of Q_G and Q_L. At a high Q_L, the increased liquid shear force accumulated at gaseous threads squeezes strongly the bubble neck. For the higher Q_G, the gaseous threads movement is significantly accelerated due to the increased U_G. Besides, the increased gas dynamic pressure could also promote the radial expansion of gas-liquid interface which slows down the movement of surrounding liquid. Both factors contribute to the faster decrease of bubble neck thickness. At the same Q_L and Q_G, δ_{neck} decreases slower with the increasing C_{MEA}. This is because the chemical absorption will affect the force balance at the gas-liquid interface. The accelerated diffusion of CO_2 molecules into the liquid phase reduces the gas dynamic pressure, resulting in the radial contraction of the gas-liquid interface. This allows the liquid phase to fill up the space around the bubble neck and to reduce the shear force. Moreover, the faster CO_2 molecular transport from liquid mass transfer layer to liquid bulk area strengthens the asymmetric molecular force in two-phase interfacial region and increases the dynamic surface tension [44,45]. In brief, the decreased shear force on upstream gas-liquid interface and the increased dynamic surface tension at high C_{MEA} slow down the bubble neck thinning, thereby inhibits the bubble pinch-off.

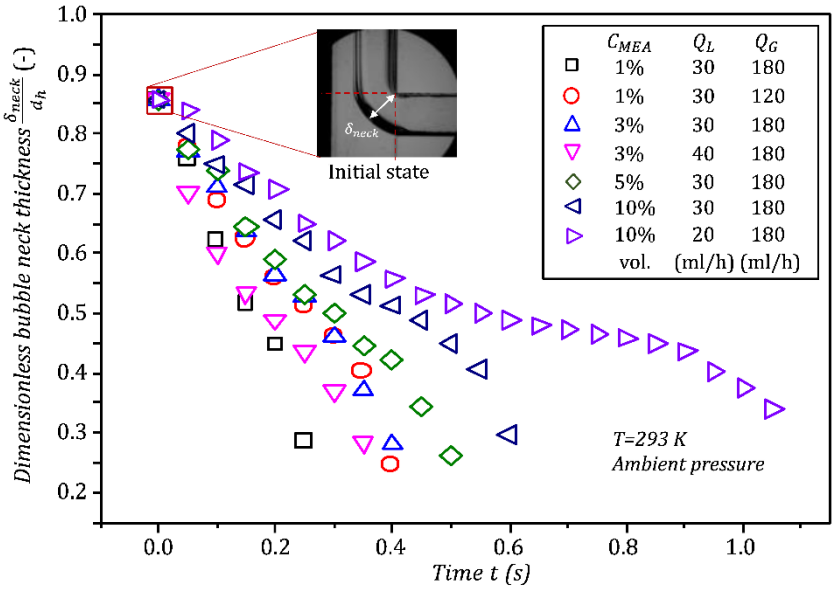

Figure 7. Evolution of dimensionless bubble neck thickness at different gas & liquid flow rates and MEA solution concentrations.

The duration of single bubble generation (τ_b) and the bubble generation frequency (f_b) are two important parameters that characterize the bubble breakup phenomenon. The former indicates the time from bubble cap entering the main channel to the bubble neck collapse whereas the latter counts the number of bubbles generated per unit time. Shown in Fig. 8 are the τ_b values as well as the duration percentage of three stages during one bubble generation under different testing conditions. It can be seen that among the three stages, the duration of bubble axial expansion in the main channel is always the longest. The increase of Q_L and C_{MEA} could both enhance the CO_2 chemical absorption, but their impact on the bubble generation is rather different. The increasing C_{MEA} will inhibit the bubble generation, evidenced by the lengthened τ_b (Fig. 8) and the reduced generation frequency (Fig. 9b). This could be attributed to two reasons. On the one hand, the fast CO_2 absorption suppresses the gas phase fore-cap velocity, lengthening the bubble penetration and expansion in the main minichannel. On the other hand, the increased chemical reaction rate inhibits the bubble neck thinning as discussed above. In contrast, the increasing U_L enhances the mass transfer, but augments also the shear force on the bubble neck, favoring the bubble neck thinning and the pinch-off.

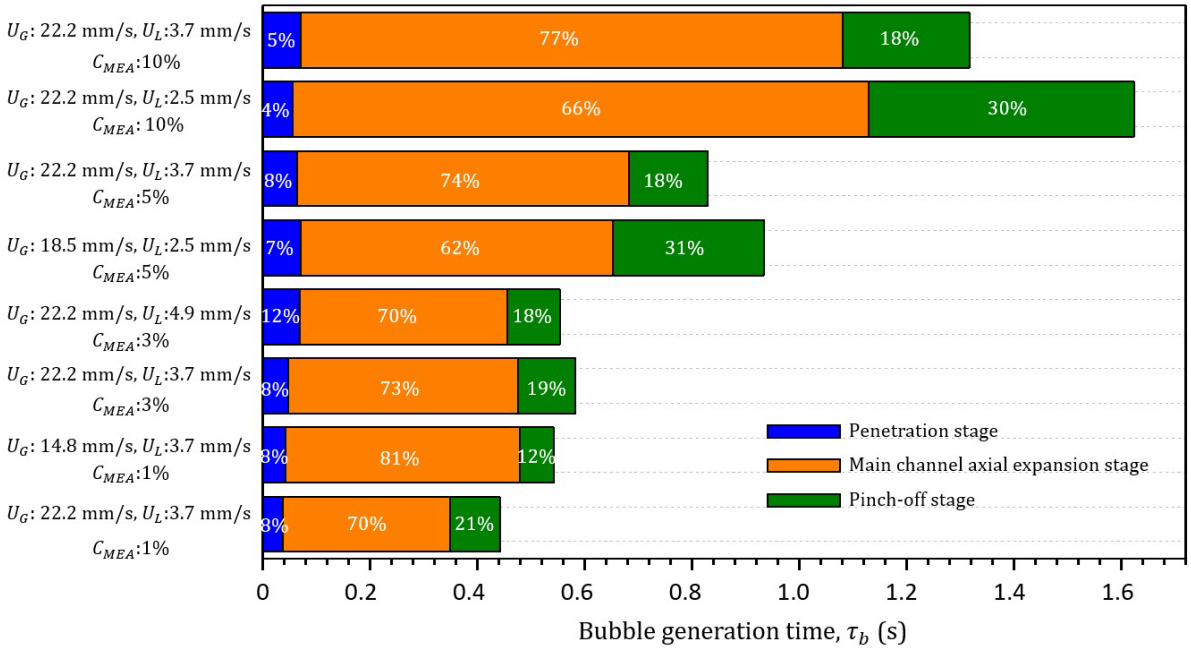

Figure 8. Effect of U_G, U_L and C_{MEA} on the duration of bubble penetration, axial expansion and pinch-off stages during one bubble generation.

Figure 9a shows that at a given C_{MEA} (1%), f_b significantly increases with the increasing U_G and U_L which is in line with the trend shown in Fig. 8. Figure 9b shows again the inhibitory effect of chemical reaction on the bubble generation. In fact, at a high C_{MEA} (10%) and a low U_G (<12

mm/s), the smaller gas supply rate than the CO_2 absorption rate could completely suppress the entry of bubble cap into the main channel. This operation mode has the maximum CO_2 deduction rate but at the cost of a low CO_2 loading efficiency of the absorbent.

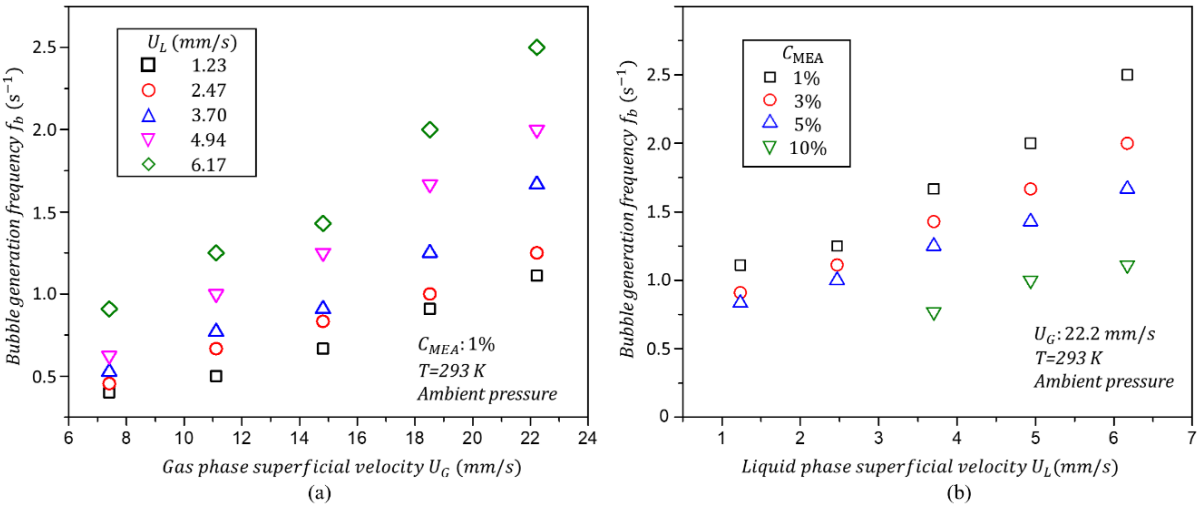

Figure 9. CO_2 bubble generation frequency f_b (s^{-1}) measured in this study. (a) Effect of U_G and U_L on f_b; (b) Effect of C_{MEA} on f_b.

3.2.2 Initial bubble length

Initial bubble length (l_0) plays a crucial role in determining the dynamic behaviors and mass transfer performance of the two-phase flow. It is also a key parameter for optimizing the size of microchannel-based CO_2 absorbers. Figure 10 reports the dimensionless initial CO_2 bubble length (l_0/d_h) optically captured and determined by image analysis in this study. It should be noted that the rear part of newly generated bubble is unstable but oscillating due to the sudden change of the surface tension [46], resulting in the fluctuation of the bubble length value right after the pinch-off. To reduce this impact of instability, the l_0/d_h value is determined when stable rear cap is formed and the mean value of l_0/d_h among bubbles generated in 20 s are presented.

Figure 10a shows that at certain C_{MEA} and U_L, l_0/d_h increases with increasing U_G because of the higher gas filling rate. In contrast, l_0/d_h decreases with the increasing U_L, especially at a high U_G (e.g., 22.2 mm/s), mainly due to the increased shear stress and the intensified absorption [39,47]. Figure 10b shows the shorter l_0/d_h at the higher C_{MEA}, indicating the strong effect of chemical absorption that should be considered.

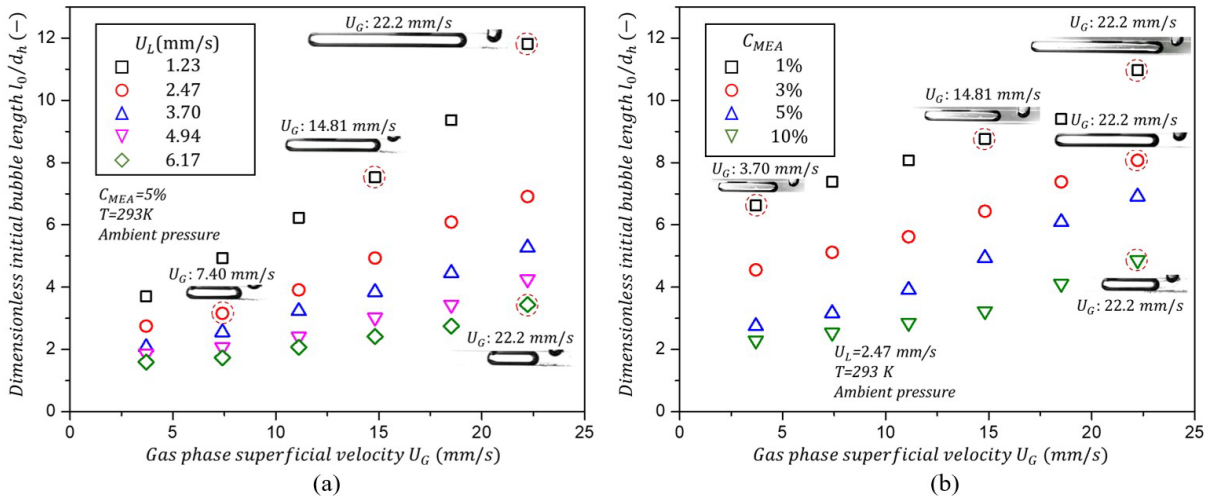

Figure 10. Measured dimensionless initial bubble length (l_0/d_h) in this study. (a) Effect of U_G and U_L on l_0/d_h; (b) Effect of C_{MEA} on l_0/d_h.

Plenty of semi-empirical correlations have been proposed to describe and predict the initial bubble length in micro/mini-channel with T-junction, some of them are listed in Table 3.

Table 3. Some initial bubble length prediction correlations proposed in the literature

Ref.	Microchannel dimensions	Fluids	Prediction model	Eq.
[48]	0.8 mm×0.8 mm L = 160 mm	Air − Ethanol	$\frac{l_0}{w_c} = 1.5 + 1.5\frac{U_G}{U_L}$	(9)
[22]	0.3 mm×0.3 mm Serpentine channel	N_2 − water	$\frac{l_0}{w_G} = 1.03(\frac{w_G \cdot w_L}{{w_c}^2})^{0.33} + 2.17(\frac{w_G}{w_L})\frac{U_G}{U_L}$	(10)
[23]	0.5 mm× 0.5 mm	Air − glycerol/water	$\frac{l_0}{w_c} = 0.5(sin\gamma\frac{Q_G}{Q_L} + 0.4cot\gamma)^{0.5}Ca_L^{-0.2}$	(11)
[17]	0.12 mm×0.04 mm L = 40 mm	N_2 − glycerol/water	$\frac{l_0}{w_c} = 1 + \frac{1}{3}\frac{Q_G}{Q_L}$	(12)
[24]	0.4 mm×0.6 mm L = 45 mm	CO_2 − MEA	$\frac{l_0}{w_c} = \frac{0.6}{Q_L/(Q_L+Q_G)}$	(13)
[19]	0.6 mm×0.3 mm	N_2 − glycerol	$\frac{l_0}{w_c} = 1.197 + 0.763Ca_L^{-0.154}\frac{U_G}{U_L}$	(14)
[49]	0.594 mm×0.08 mm Serpentine channel	Air − Water	$\frac{l_0}{w_c} = 1 + 1.724{Re_{TP}}^{0.173}(\frac{U_G}{U_L})^{0.797}$	(15)
[26]	0.4 mm×0.4 mm	CO_2 − MEA	$\frac{l_0}{w_c} = 0.36 + 1.88{Re_{TP}}^{-0.14}(1+Ha)^{-0.09}(\frac{Q_G}{Q_L})^{0.76}$	(16)

γ: Gas-liquid contact angle.
w_G, w_L *and* w_C: Width of the gas inlet, the liquid inlet, and the main channel, respectively.
Re_{TP}: Two-phase flow Reynolds number, $Re_{TP} = \rho_L(U_L + U_G)d_h/\mu_L$.

Nevertheless, most of these correlations were developed for physical absorption dominated two-phase flow system, causing significant errors when being used for CO_2 chemical absorption, as shown in Fig. 11a. Zhu et al. [24] experimentally investigated the CO_2-MEA chemical absorption in microchannel and demonstrated the effect of chemical reaction on bubble formation. However, the prediction correlation proposed (Eq. 13) is only based on the gas and liquid flowrates while chemical reaction-related parameters are absent. Worth-noting is the study of Yin et al. [26] in which an l_0 prediction correlation (Eq. 16) has been proposed by additionally introducing the chemical reaction-related Ha number (Eq. 17).

$$\frac{l_0}{w_c} = 0.36 + 1.88{Re_{TP}}^{-0.14}(1+Ha)^{-0.09}(\frac{Q_G}{Q_L})^{0.76} \tag{16}$$

$$Ha = \sqrt{Dk_{ov}/{k_L}^2} \tag{17}$$

where D is two-phase diffusion rate (m^2/s), k_{ov} is overall chemical reaction kinetic constant (s^{-1}), k_L is physical absorption mass transfer coefficient (m/s) and determined by the permeation model [50]:

$$k_L = \sqrt{D/\pi\tau_b} \tag{18}$$

where τ_b (s) is bubble formation duration that needs to be estimated by imaging and data processing. Therefore, the calculation of Ha number could be complicated, laborious, and sometimes inaccurate, rendering the prediction correlation difficult to use in practice. Moreover, the comparison between model predicted results based on Eq.16 and experimental data sets obtained in this study shows clearly a discrepancy (Fig. 11b): the impact of C_{MEA} on l_0/d_h values cannot be well reflected.

Here we propose to build a new prediction model by including the easier-to-use Damköhler number (Da), the gas-liquid superficial velocity ratio (U_G/U_L), and the Ca number, as shown in Eq. (19):

$$\frac{l_0}{d_h} = \frac{a(1+(U_G/U_L)^b)Ca^c}{1+Da^d} \tag{19}$$

$$Da = k_{ov}\cdot {d_h}^2/D \tag{20}$$

$$Ca = \mu U/\sigma \tag{21}$$

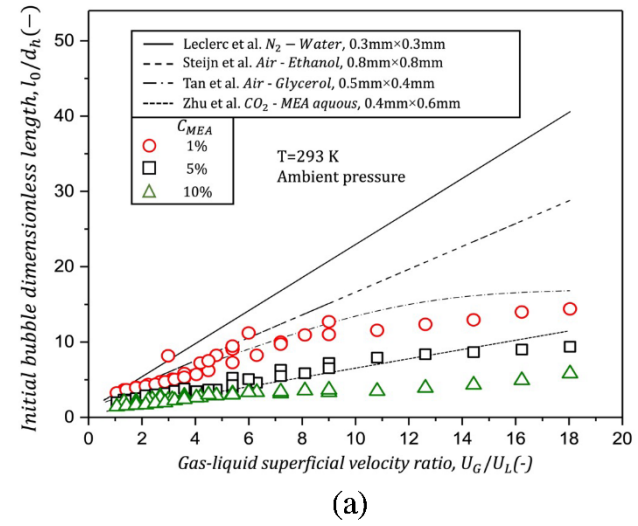

(a)

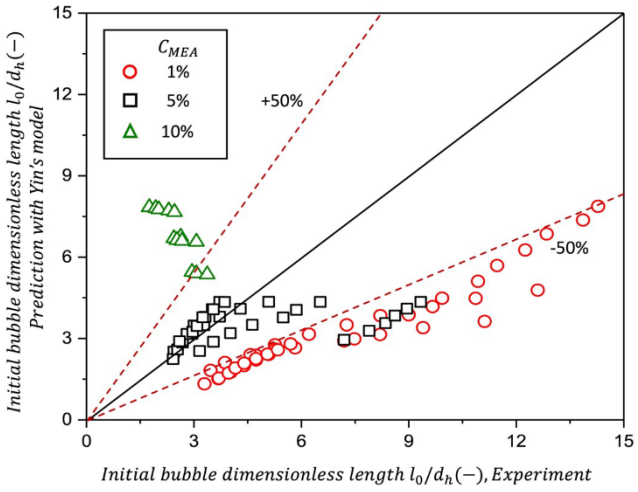

(b)

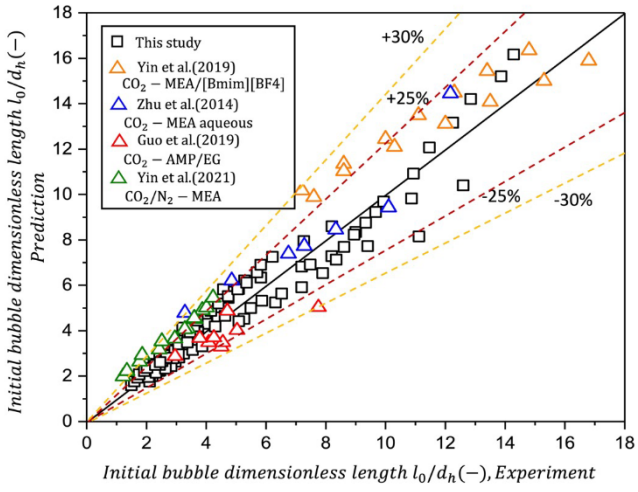

(c)

Figure 11. Dimensionless initial bubble length and prediction model. (a)(b) Comparison between l_0/d_h prediction models without and with chemical reaction related parameter and experimental data in this study; (c) Comparison between the *Da* number-based model proposed in this study and experimental data in the literature using different absorbents.

In this new prediction model, Da number (Eq. 20) is defined as the ratio of kinetic constant (k_{ov}) to diffusion rate (D), which could jointly reflect the influences of chemical reaction and diffusion mass transfer [25]. It can be easily calculated from the physio-chemical properties of two-phase flow system, thereby more straightforward than the *Ha* number. The higher the absorbent concentration (thus higher *Da* number), the shorter Taylor bubbles will be generated. U_G/U_L characterizes the hydrodynamics of the gas-liquid two-phase flow system and the Ca number (Eq. 21) reflects the relative effect of viscous drag force and the surface tension force on the gas-liquid interface.

Fitting constants (*a*=146.4; *b*=0.67; *c*=-0.07; *d*=0.38) were calculated based on the experimental data obtained in this study, showing a good prediction accuracy with the relative prediction error smaller than ±25% (95% confidence interval). Further comparisons and verifications using experimental data from Yin et al. [26,30], Zhu et al. [24], and Guo et al. [51] are also presented in Fig. 11c. A good agreement (relative error< ±30%) can be seen between the prediction values using our correlation (Eq. 19) and fitting constants and the experimental data in the literature using different absorbents.

3.3 Bubble moving in the main channel

The initial CO_2 Taylor bubble, once formed through the T-junction, will move and gradually shrink in the minichannel due to chemical absorption. For straight channel without change of cross-section geometry and dimension, the bubble dynamics could be characterized by the bubble length decrease rate and the bubble moving velocity, discussed in detail in this sub-section.

3.3.1 Bubble length decrease rate

The transient bubble length decrease rate is defined as the Taylor bubble length variation ($\Delta l_t = l_t - l_{t+\Delta t}$) within a certain time interval (Δt), before the sphere bubble is formed at the end of absorption. Recall that in this study l_t and $l_{t+\Delta t}$ were captured by high-speed camera and calculated by image analysis with time interval $\Delta t = 0.1$ s. The relative bubble length lost is also introduced for discussion, defined as the ratio of shrunk bubble length ($l_0 - l_t$) to the initial bubble length l_0.

Figure 12 presents the evolution of relative bubble length lost ($1 - l_t/l_0$) and the transient bubble length decrease rate ($\Delta l_t/\Delta t$) as a function of the bubble moving time (t) under different Re_G, Re_L and C_{MEA} conditions. It could be observed that ($1 - l_t/l_0$) increases rapidly at the

early stage of bubble absorption, especially under high Re_L and C_{MEA}. Later, it slows down and stabilizes, mainly due to the decreased mass transfer rate caused by the reduced CO_2 concentration gradient around the bubble [52,53] and the smaller interfacial areas. For the same reason, the bubble length decrease rate gradually drops towards zero with the transition of flow pattern from slug flow to bubbly flow. Increasing Re_G and Re_L both augment the bubble length decrease rate due to the enhanced mass transfer, as shown in Fig. 12a. Unsuperisingly, higher C_{MEA} promotes the bubble shrinkage due to the increased chemical reaction rate, as shown in Fig. 12b.

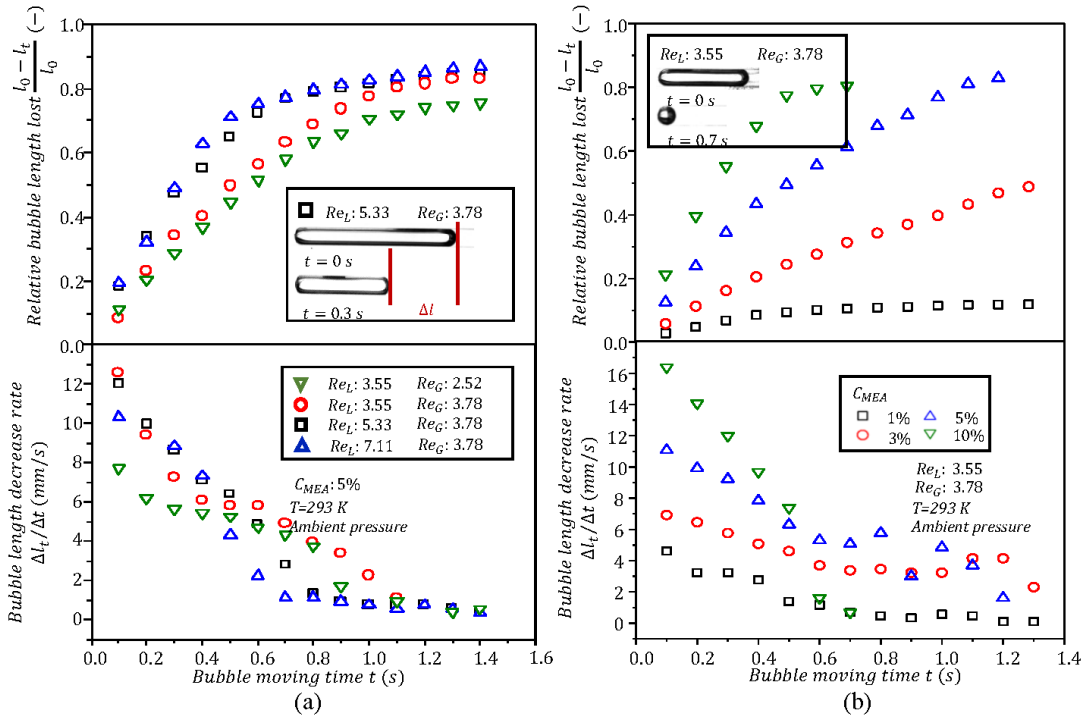

Figure 12. Relative bubble length lost ($1 - l_t/l_0$) and bubble length decrease rate ($\Delta l_t/\Delta t$) as a function of bubble moving time (t) in minichannel. (a) Effect of gas & liquid Re numbers; (b) Effect of absorbent concentration (C_{MEA}).

3.3.2 Bubble moving velocity

Figure 13 presents the bubble velocity as a function of moving time in the minichannel. Recall that in this study, the bubble velocity (v_b) is calculated as the average between the bubble rear cap velocity ($v_{r,t}$) and the bubble front cap velocity ($v_{f,t}$): $v_b = (v_{r,t} + v_{f,t})/2$. V-shape curves can be observed, indicating two stages of bubble velocity in a vertical minichannel. In the first decelerating stage, the bubble velocity tends to decrease due to the absorption of CO_2 into the liquid phase. $v_{r,t}$ is always bigger than $v_{f,t}$ because of the consistent contraction

direction with the bubble moving in the minichannel. The difference is highlighted in Fig. 13a, under the condition of $Q_G = 180$ ml/h, $Q_L = 40$ ml/h, and $C_{MEA} = 3\%$. The second accelerating stage occurs when most of CO_2 molecules are absorbed into the liquid phase and small spherical bubble is formed. The sharp drop of drag force due to nearly disappeared liquid film surrounding the bubble leads to the detachment of the small spherical bubbles from the channel wall. Driven by both the liquid phase flow and the buoyancy force, the spherical bubbles accelerate towards the channel outlet. Since the bubble length doesn't change much for small spherical bubbles, $v_{r,t}$ and $v_{f,t}$ are very close at this accelerating stage, and are equal to v_b, as shown in Fig. 13a.

Figure 13b and c show the effect of operating conditions on the variation of v_b. The decelerating and accelerating stages can still be identified at different U_L, U_G and C_{MEA} conditions. It can also be seen from Fig. 13b that the v_b value at minichannel outlet is almost decided by U_L: lower U_L leads to smaller v_b at the channel outlet. The effect of C_{MEA} on v_b is shown in Fig. 13c. For the given U_G and U_L, higher C_{MEA} results in the lower initial v_b and the earlier transition to the bubble accelerating stage due to the higher absorption rate.

From the above discussion, it can be seen that the bubble length decrease rate ($\Delta l_t/\Delta t$) and the bubble velocity (v_b), both parameters reflect the transient two-phase mass transfer rate due to chemical reaction, and their relationship needs further investigation. Some attempts have been performed in the literature by both numerical simulation [46,54] and experimental testing [55] approaches. For example, Yin et al. [30] related the bubble length reduction rate ($\Delta l/l_0$) to the transient bubble velocity using the two-phase velocity (U_{TP}): $v_b/U_{TP} = 1.29(1 - \Delta l/l_0)$. This empirical model is focus on the accumulated bubble length change but gives little hint on the chemical reaction impacted bubble transient dynamics. Therefore, a more precise correlation that couples v_b and $\Delta l_t/\Delta t$ is still lacking.

Figure 14a plots the data sets of this experimental study under different Re_G, Re_L and C_{MEA} conditions, showing clearly the strong dependence of $\Delta l_t/\Delta t$ on v_b. An approximately linear regression relationship between these two parameters could be found, with its slope determined by C_{MEA}. As a result, an empirical correlation (Eq. 22) is proposed by including the Da number to indicate the impact of chemical reaction, which has not been explicitly specified before:

$$\frac{\Delta l_t}{\Delta t} = aDa \quad v_b \tag{22}$$

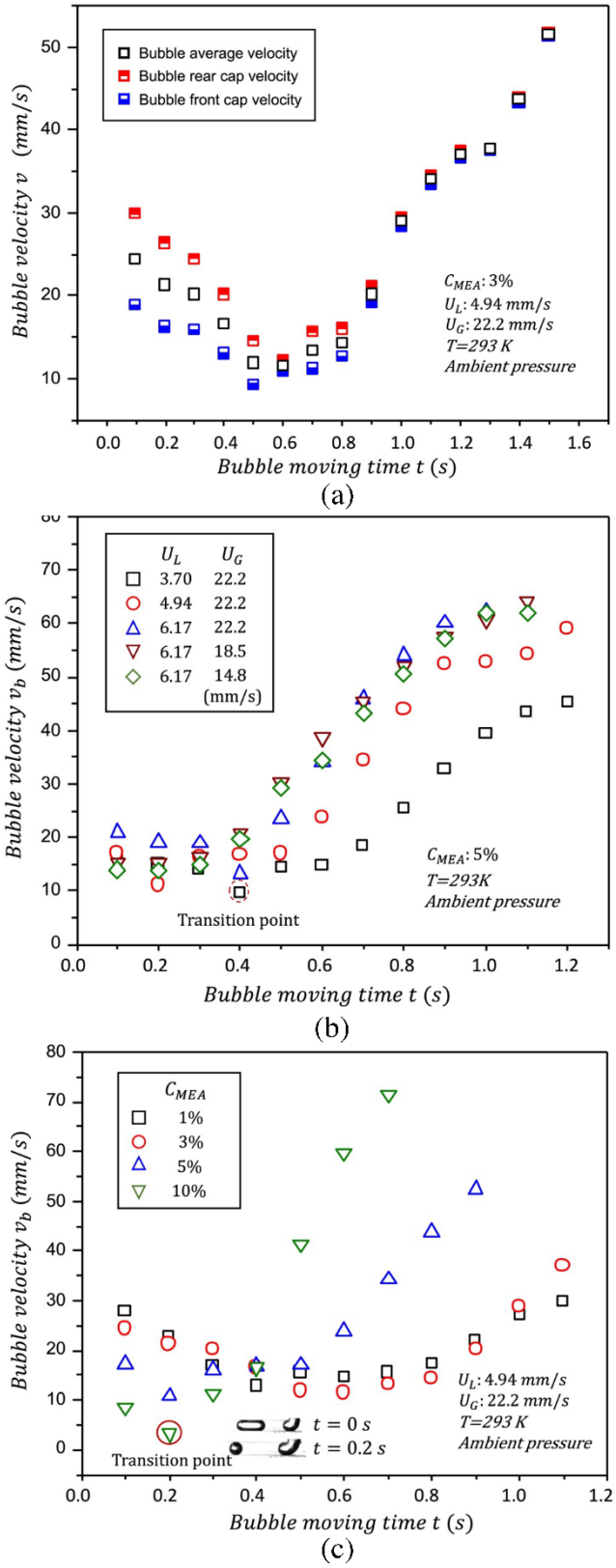

Figure 13. Bubble velocity v_b as a function of bubble moving time (t) in minichannel. (a) An example of bubble rear and front cap velocity variation at decelerating and accelerating stages; (b) Effect of U_L and U_G on v_b; (c) Effect of C_{MEA} on v_b.

The value of fitting constant (a =2.35 × 10^{-7}) was obtained based on the current data-set. Fig. 14b shows that experimental data and prediction results of this correlation are in good agreement with relative error in the range of -35%~+30% for more than 90% of the data points. This correlation fits only the bubble decelerating stage but not covers the accelerating stage. For the latter, $\Delta l_t/\Delta t$ approaches to 0 while v_b still rises as shown above. Better prediction accuracy is viable by including other physical or chemical parameters, or by a more sophisticated expression of v_b, but the simplicity of the model (Eq. 22) will be lost.

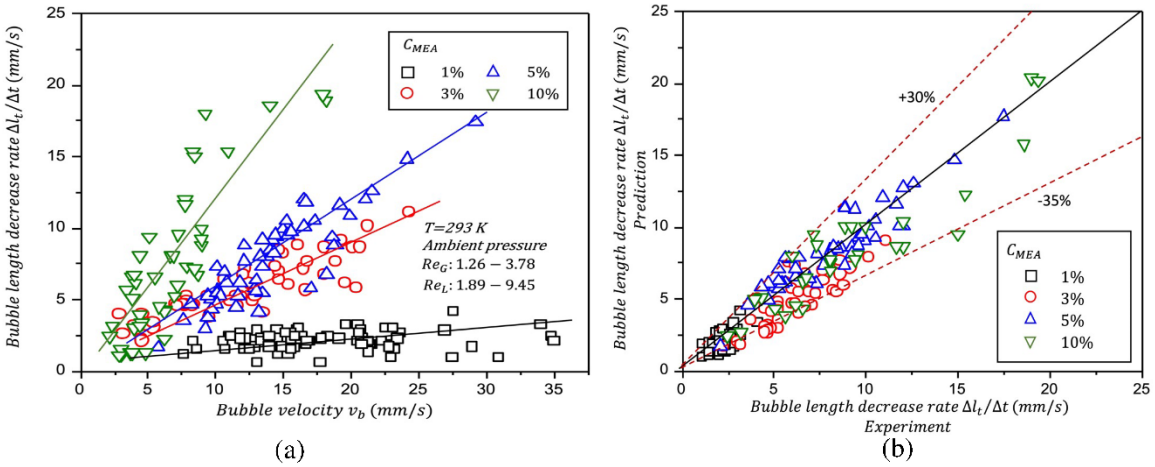

Figure 14. Bubble length decrease rate $\Delta l_t/\Delta t$ vs. bubble velocity v_b at the decelerating stage. (a) Effect of absorbent concentration (C_{MEA}); (b) Comparison of $\Delta l_t/\Delta t$ values between experimental data and model prediction results.

3.4 Effective length of microchannel

The microchannel length utilization is totally different under different gas-liquid flow rates and absorbent concentrations. This parameter should be carefully decided when designing microchannel-based CO_2 absorbers in real practice. Here we introduce the notion of effective length (L_e) of micro/minichannel CO_2 absorber as the distance from the T-junction to the point where the slug bubble shrinks into spherical bubble ($l_b = d_h$), as illustrated in Fig. 15. Most of the CO_2 is absorbed within this channel length and after that point, the bubble volume change becomes relatively minor thus the channel length unitization is less efficient. The dimensionless effective length (L_e^*) is then defined as the ratio of L_e to the hydraulic diameter (d_h) of the channel (Eq. 23).

$$L_e^* = \frac{L_e}{d_h} \tag{23}$$

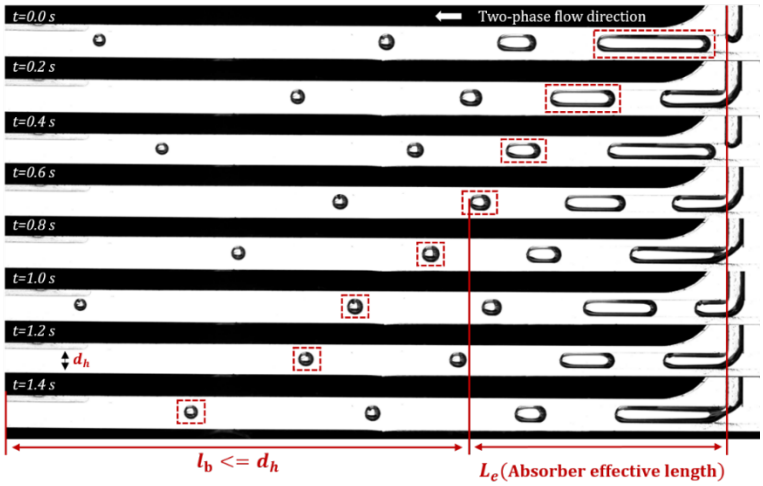

Figure 15. Schematic diagram for the effective length of the micro/minichannel CO_2 absorber.

Figure 16a and 16b presents the L_e^* values obtained under different U_G, U_L and C_{MEA} conditions in this study. Clearly, L_e^* value decreases with the increasing C_{MEA} because of the shorter initial bubble length l_0 (cf. Fig. 10b) at the bubble generation stage and the higher bubble length decrease rate (cf. Fig. 12b) at the bubble moving stage. At a high C_{MEA} (e.g., 10%), the impact of U_G and U_L on L_e^* becomes minor, as shown in Fig. 16b. At a lower C_{MEA}, the positive effect of U_L on the reduction of L_e^* can be seen. In contrast, the effect of U_G is more complicated. The increased Q_G elongates l_0 but also enhances the gas-liquid mass transfer. As a result, at a low C_{MEA} (such as 3%) and U_L (such as 1.23 mm/s), the two-phase mass transfer performance is limited and increased l_0 requests longer L_e^*. With the increase of U_L, the enhanced mass transfer greatly augments the bubble length decrease rate, L_e^* varies little with the increasing U_G.

Based on the experimental data of this study, a simple predicting model (Eq. 24) is proposed in the first time to facilitate the engineering calculation. This model could be used either to predict the effective channel length based on the known operating conditions when designing a new CO_2 absorber, or in the opposite case, to determine the suitable range of operating condition parameters for an existing microchannel-based absorber. Da and Ca numbers as well as the velocity ratio (U_G/U_L), key parameters that determine the Taylor bubble dynamics at both the bubble generation and moving stages, are included to consider effects of chemical reaction and physical parameters on L_e^* for micro/minichannel absorbers.

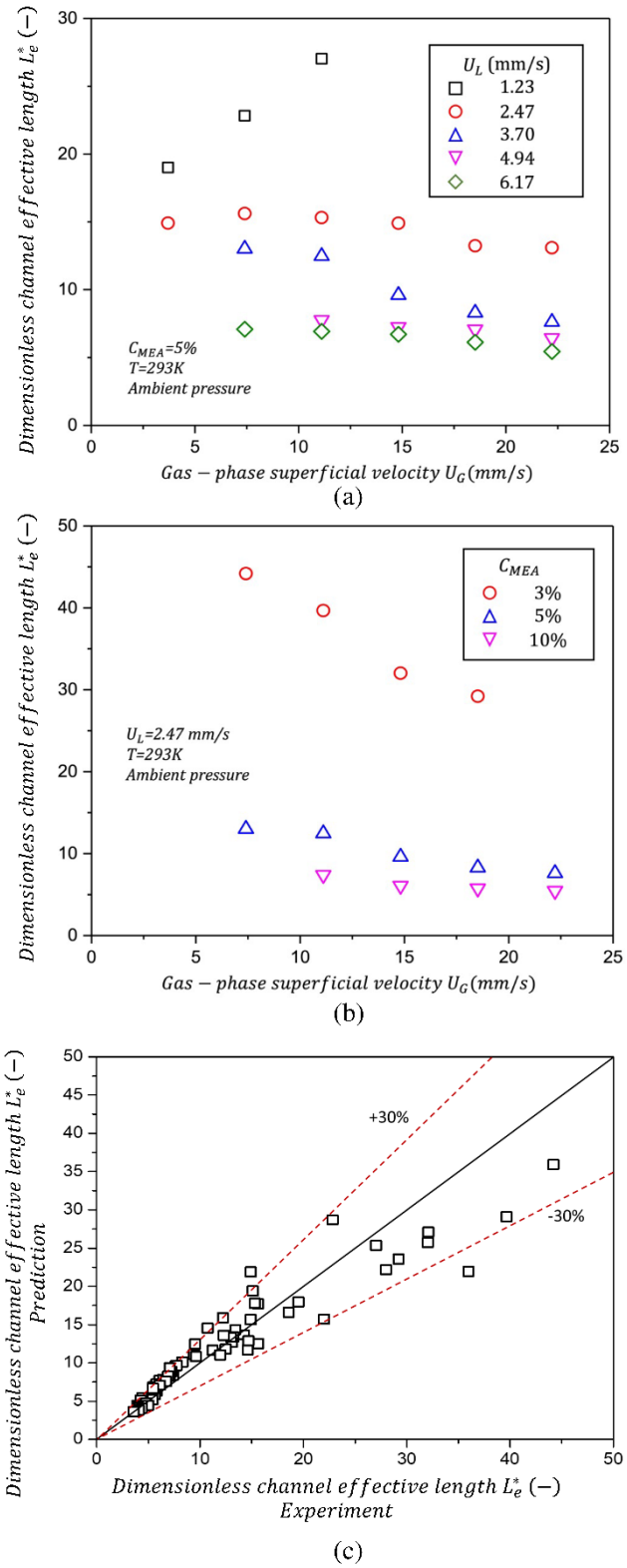

Figure 16. Dimensionless channel effective length L_e^* proposed and determined in this study. (a) Effect of U_G & U_L; (b) Effect of C_{MEA}; (c) Comparison of L_e^* values between experimental data and model prediction results.

$$L_e^* = a\frac{(U_G/U_L)^b}{CaDa}(U_G < 22\ mm/s, U_L < 6.17\ mm/s) \quad (24)$$

Fitting constants ($a = 4.07 \times 10^3$ and $b = -0.304$) were calculated based on the experimental data of this study. The prediction results using this model show a good accuracy, with relative error smaller than ±30% for 90% of the data points.

4. Conclusion and perspectives

In this study, experiments of CO_2 absorption by MEA aqueous solution in a straight minichannel with T-junction were performed under different gas and liquid flow rates and absorbent concentrations. Taylor bubble dynamics under chemical reaction-enhanced mass transfer were characterized and analyzed, including two-phase flow patterns, bubble generation, its moving and shrinkage. Main conclusions obtained are summarized as follows:

- Chemical reaction-enhanced mass transfer inhibits the Taylor bubble generation in the minichannel. The intensified CO_2 absorption at high C_{MEA} hinders the bubble cap penetration and expansion in the main channel on one hand, and alleviates the bubble neck thinning on the other hand, resulting in the lengthened bubble generation duration and the reduced bubble generation frequency.
- A new correlation (Eq. 19) based on U_G/U_L, Da number and Ca number has been proposed to predict the initial Taylor bubble length (l_0) in minichannel under chemical reaction-enhanced mass transfer. Comparison with experimental data in the literature using different absorbents shows good prediction accuracy of the proposed correlation.
- Once generated, the Taylor bubble first decelerates and shrinks into spherical shape due to strong chemical absorption, and then detaches from the channel wall and accelerates towards the minichannel outlet. An approximately linear regression relationship can be seen between bubble length decrease rate ($\frac{\Delta l_t}{\Delta t}$) and the bubble velocity (v_b) before the transition to spherical bubble, with the slop determined by C_{MEA}. An empirical correlation (Eq. 22) based on Da number has been developed to relate these two bubble dynamic parameters.
- The notion of effective channel length for CO_2 absorption has been put forward and a simple model (Eq. 24) has been proposed to facilitate the engineering calculation. This

model could be useful for the design of microchannel CO_2 absorbers and for determining their suitable range of operating conditions.

The obtained and characterized Taylor bubble dynamic parameters can be used to further analyze the two-phase mass transfer behaviors in microchannel-based absorber under chemical reaction, which is our on-going work. Moreover, the hydrodynamic and mass transfer behaviors of the liquid phase, also essential in understanding the CO_2 chemical absorption in microchannel, need to be investigated in detail. Therefore, our next goal will be focused on the real-time and accurate experimental measurement of velocity field and CO_2 concentration distribution in the liquid phase, as well as their dynamic behaviors under chemical reaction-enhanced mass transfer. This will provide new insights into the understanding of two-phase transport phenomena in microchannel.

Acknowledgement

This work is supported by China Scholarship Council with the scholarship for Mr. Hao CHENG (No. 20200673006).

References

[1] D. Gao, Y. Qi, J. Yang, H. Zhang, Experimental study of carbon dioxide desorption from ethanolamine/non-aqueous CO2-rich absorbent solvent using microchannel, Sep. Purif. Technol. 331 (2024) 125651. https://doi.org/10.1016/j.seppur.2023.125651.

[2] L. He, Y. Fan, J. Bellettre, J. Yue, L. Luo, Catalytic methane combustion in plate-type microreactors with different channel configurations: An experimental study, Chem. Eng. Sci. 236 (2021) 116517. https://doi.org/10.1016/j.ces.2021.116517.

[3] H. Cheng, H. Liu, W. Li, M. Li, Recent advances in magnetic digital microfluidic platforms, Electrophoresis. 42 (2021) 2329–2346. https://doi.org/10.1002/elps.202100088.

[4] L. Chen, G. Msigwa, M. Yang, A.I. Osman, S. Fawzy, D.W. Rooney, P.-S. Yap, Strategies to achieve a carbon neutral society: a review, Environ. Chem. Lett. 20 (2022) 2277–2310. https://doi.org/10.1007/s10311-022-01435-8.

[5] H. Cheng, Y. Fan, D. Tarlet, L. Luo, Z. Fan, Microfluidic-based chemical absorption technology for CO2 capture: Mass transfer dynamics, operating factors and performance intensification, Renew. Sustain. Energy Rev. 181 (2023) 113357. https://doi.org/10.1016/j.rser.2023.113357.

[6] M. Pasha, S. Liu, J. Zhang, M. Qiu, Y. Su, Recent Advancements on Hydrodynamics and Mass Transfer Characteristics for CO 2 Absorption in Microreactors, Ind. Eng. Chem. Res. 61 (2022) 12249–12268. https://doi.org/10.1021/acs.iecr.2c01982.

[7] M. Pasha, G. Li, M. Shang, S. Liu, Y. Su, Mass transfer and kinetic characteristics for CO2 absorption in microstructured reactors using an aqueous mixed amine, Sep. Purif. Technol. 274 (2021) 118987. https://doi.org/10.1016/j.seppur.2021.118987.

[8] Y. Zhang, C. Zhu, T. Fu, X. Gao, Y. Ma, H.Z. Li, CO2 absorption and desorption performance by ChCl-MEA-PZ deep eutectic solvent aqueous solutions, Sep. Purif. Technol. 330 (2024) 125275. https://doi.org/10.1016/j.seppur.2023.125275.

[9] T. Zhang, B. Cao, Y. Fan, Y. Gonthier, L. Luo, S. Wang, Gas-liquid flow in circular microchannel. Part I: Influence of liquid physical properties and channel diameter on flow patterns, Chem. Eng. Sci. 66 (2011) 5791–5803. https://doi.org/10.1016/j.ces.2011.07.035.

[10] H. Niu, L. Pan, H. Su, S. Wang, Flow Pattern, Pressure Drop, and Mass Transfer in a Gas−Liquid Concurrent Two-Phase Flow Microchannel Reactor, Ind. Eng. Chem. Res. 48 (2009) 1621–1628. https://doi.org/10.1021/ie801095a.

[11] Y. Yin, W. Chen, C. Wu, X. Zhang, T. Fu, C. Zhu, Y. Ma, Bubble dynamics and mass transfer enhancement in split–and–recombine (SAR) microreactor with rapid chemical reaction, Sep. Purif. Technol. 287 (2022) 120573. https://doi.org/10.1016/j.seppur.2022.120573.

[12] Y. Zhou, C. Yao, P. Zhang, X. Zhang, H. Lü, Y. Zhao, Dynamic Coupling of Mass Transfer and Chemical Reaction for Taylor Flow along a Serpentine Microchannel, Ind. Eng. Chem. Res. 59 (2020) 9279–9292. https://doi.org/10.1021/acs.iecr.0c00014.

[13] L. Zheng, B. Zhang, Y. Luo, K. Guo, Z. Wang, K. Liu, X. Mei, C. Liu, Mass transfer dynamics of single CO2 bubbles rising in monoethanolamine solutions: Experimental study and mathematical model, Chem. Eng. J. 465 (2023) 142761. https://doi.org/10.1016/j.cej.2023.142761.

[14] C. Chu, F. Zhang, C. Zhu, T. Fu, Y. Ma, Mass transfer characteristics of CO2 absorption into 1-butyl-3-methylimidazolium tetrafluoroborate aqueous solution in microchannel, Int. J. Heat Mass Transf. 128 (2019) 1064–1071. https://doi.org/10.1016/j.ijheatmasstransfer.2018.09.077.

[15] Y. Zhao, G. Chen, C. Ye, Q. Yuan, Gas-liquid two-phase flow in microchannel at elevated pressure, Chem. Eng. Sci. 87 (2013) 122–132. https://doi.org/10.1016/j.ces.2012.10.011.

[16] Z. Yu, O. Hemminger, L.-S. Fan, Experiment and lattice Boltzmann simulation of two-phase gas–liquid flows in microchannels, Chem. Eng. Sci. 62 (2007) 7172–7183. https://doi.org/10.1016/j.ces.2007.08.075.

[17] T. Fu, Y. Ma, D. Funfschilling, C. Zhu, H.Z. Li, Squeezing-to-dripping transition for bubble formation in a microfluidic T-junction, Chem. Eng. Sci. 65 (2010) 3739–3748. https://doi.org/10.1016/j.ces.2010.03.012.

[18] V. van Steijn, C.R. Kleijn, M.T. Kreutzer, Flows around Confined Bubbles and Their Importance in Triggering Pinch-Off, Phys. Rev. Lett. 103 (2009) 214501. https://doi.org/10.1103/PhysRevLett.103.214501.

[19] C. Yao, J. Zheng, Y. Zhao, Q. Zhang, G. Chen, Characteristics of gas-liquid Taylor flow with different liquid viscosities in a rectangular microchannel, Chem. Eng. J. 373 (2019) 437–445. https://doi.org/10.1016/j.cej.2019.05.051.

[20] L. Sheng, Y. Chang, J. Deng, G. Luo, Taylor Bubble Generation Rules in Liquids with a Higher Viscosity in a T-Junction Microchannel, Ind. Eng. Chem. Res. 61 (2022) 2623–2632. https://doi.org/10.1021/acs.iecr.1c05015.

[21] P. Garstecki, M.J. Fuerstman, H.A. Stone, G.M. Whitesides, Formation of droplets and bubbles in a microfluidic T-junction—scaling and mechanism of break-up, Lab Chip. 6 (2006) 437. https://doi.org/10.1039/b510841a.

[22] A. Leclerc, R. Philippe, V. Houzelot, D. Schweich, C. de Bellefon, Gas–liquid Taylor flow in square micro-channels: New inlet geometries and interfacial area tuning, Chem. Eng. J. 165 (2010) 290–300. https://doi.org/10.1016/j.cej.2010.08.021.

[23] J. Tan, S.W. Li, K. Wang, G.S. Luo, Gas–liquid flow in T-junction microfluidic devices with a new perpendicular rupturing flow route, Chem. Eng. J. 146 (2009) 428–433. https://doi.org/10.1016/j.cej.2008.10.024.

[24] C. Zhu, C. Li, X. Gao, Y. Ma, D. Liu, Taylor flow and mass transfer of CO2 chemical absorption into MEA aqueous solutions in a T-junction microchannel, Int. J. Heat Mass Transf. 73 (2014) 492–499. https://doi.org/10.1016/j.ijheatmasstransfer.2014.02.040.

[25] D. Ma, C. Zhu, T. Fu, X. Yuan, Y. Ma, An effective hybrid solvent of MEA/DEEA for CO2 absorption and its mass transfer performance in microreactor, Sep. Purif. Technol. 242 (2020) 116795. https://doi.org/10.1016/j.seppur.2020.116795.

[26] Y. Yin, X. Zhang, C. Zhu, T. Fu, Y. Ma, Formation characteristics of Taylor bubbles in a T-junction microchannel with chemical absorption, Chinese J. Chem. Eng. 46 (2022) 214–222. https://doi.org/10.1016/j.cjche.2021.06.002.

[27] N. Shao, A. Gavriilidis, P. Angeli, Mass transfer during Taylor flow in microchannels with and without chemical reaction, Chem. Eng. J. 160 (2010) 873–881. https://doi.org/10.1016/j.cej.2010.02.049.

[28] J. Tan, Y.C. Lu, J.H. Xu, G.S. Luo, Mass transfer performance of gas–liquid segmented flow in microchannels, Chem. Eng. J. 181–182 (2012) 229–235. https://doi.org/10.1016/j.cej.2011.11.067.

[29] R. Dong, D. Chu, Q. Sun, Z. Jin, Numerical simulation of the mass transfer process of <scp> CO $_2$ </scp> absorption by different solutions in a microchannel, Can. J. Chem. Eng. 98 (2020) 2648–2664. https://doi.org/10.1002/cjce.23781.

[30] Y. Yin, T. Fu, C. Zhu, R. Guo, Y. Ma, H. Li, Dynamics and mass transfer characteristics of CO2 absorption into MEA/[Bmim][BF4] aqueous solutions in a microchannel, Sep. Purif. Technol. 210 (2019) 541–552. https://doi.org/10.1016/j.seppur.2018.08.045.

[31] P.V. Danckwerts, The reaction of CO2 with ethanolamines, Chem. Eng. Sci. 34 (1979) 443–446. https://doi.org/10.1016/0009-2509(79)85087-3.

[32] B. Aghel, E. Heidaryan, S. Sahraie, M. Nazari, Optimization of monoethanolamine for CO2 absorption in a microchannel reactor, J. CO2 Util. 28 (2018) 264–273. https://doi.org/10.1016/j.jcou.2018.10.005.

[33] L.J. Du Preez, J.P. Barnard, L.H. Callanan, J.H. Knoetze, Reaction Kinetics of CO 2 with Monoethanolamine in n -Propanol. 1. Reaction Kinetic Data and Comparison with Existing Rate Law Expressions, Ind. Eng. Chem. Res. 57 (2018) 9716–9724. https://doi.org/10.1021/acs.iecr.8b01482.

[34] H. Cheng, D. Tarlet, Y. Fan, L. Luo, Mass transfer enhancement for CO2 chemical absorption in a spiral baffle embedded microchannel, Chem. Eng. Sci. 280 (2023) 118968. https://doi.org/10.1016/j.ces.2023.118968.

[35] L.W. Sumner, A. Amberg, D. Barrett, M.H. Beale, R. Beger, C.A. Daykin, T.W.-M. Fan, O. Fiehn, R. Goodacre, J.L. Griffin, T. Hankemeier, N. Hardy, J. Harnly, R. Higashi, J. Kopka, A.N. Lane, J.C. Lindon, P. Marriott, A.W. Nicholls, M.D. Reily, J.J. Thaden, M.R. Viant, Proposed minimum reporting standards for chemical analysis, Metabolomics. 3 (2007) 211–221. https://doi.org/10.1007/s11306-007-0082-2.

[36] R.J. Moffat, Describing the uncertainties in experimental results, Exp. Therm. Fluid Sci. 1 (1988) 3–17. https://doi.org/10.1016/0894-1777(88)90043-X.

[37] A. Kawahara, P.M.-Y. Chung, M. Kawaji, Investigation of two-phase flow pattern, void fraction and pressure drop in a microchannel, Int. J. Multiph. Flow. 28 (2002) 1411–1435. https://doi.org/10.1016/S0301-9322(02)00037-X.

[38] F. Guo, B. Chen, Numerical Study on Taylor Bubble Formation in a Micro-channel T-Junction Using VOF Method, Microgravity Sci. Technol. 21 (2009) 51–58. https://doi.org/10.1007/s12217-009-9146-4.

[39] S. Haase, Characterisation of gas-liquid two-phase flow in minichannels with co-flowing fluid injection inside the channel, part II: gas bubble and liquid slug lengths, film thickness, and void fraction within Taylor flow, Int. J. Multiph. Flow. 88 (2017) 251–269. https://doi.org/10.1016/j.ijmultiphaseflow.2016.09.002.

[40] J. Tan, L. Du, J.H. Xu, K. Wang, G.S. Luo, Surfactant-free microdispersion process of gas in organic solvents in microfluidic devices, AIChE J. 57 (2011) 2647–2656. https://doi.org/10.1002/aic.12487.

[41] H.J. Richter, Separated two-phase flow model: application to critical two-phase flow, Int. J. Multiph. Flow. 9 (1983) 511–530. https://doi.org/10.1016/0301-9322(83)90015-0.

[42] K. Yamamoto, S. Ogata, Effects of T-junction size on bubble generation and flow instability for two-phase flows in circular microchannels, Int. J. Multiph. Flow. 49 (2013) 24–30. https://doi.org/10.1016/j.ijmultiphaseflow.2012.09.002.

[43] L. Dai, W. Cai, F. Xin, Numerical Study on Bubble Formation of a Gas-Liquid Flow in a T-Junction Microchannel, Chem. Eng. Technol. 32 (2009) 1984–1991. https://doi.org/10.1002/ceat.200900351.

[44] L. Yang, G. Liu, S. Luo, K. Wang, G. Luo, Investigation of dynamic surface tension in gas–liquid absorption using a microflow interfacial tensiometer, React. Chem. Eng. 2 (2017) 232–238. https://doi.org/10.1039/C6RE00191B.

[45] L. Boubendir, S. Chikh, L. Tadrist, On the surface tension role in bubble growth and detachment in a micro-tube, Int. J. Multiph. Flow. 124 (2020) 103196. https://doi.org/10.1016/j.ijmultiphaseflow.2019.103196.

[46] H.W. Jia, P. Zhang, Investigation of the Taylor bubble under the effect of dissolution in microchannel, Chem. Eng. J. 285 (2016) 252–263. https://doi.org/10.1016/j.cej.2015.09.102.

[47] E. V Rebrov, Two-phase flow regimes in microchannels, Theor. Found. Chem. Eng. 44 (2010) 355–367. https://doi.org/10.1134/S0040579510040019.

[48] V. van Steijn, M.T. Kreutzer, C.R. Kleijn, μ-PIV study of the formation of segmented flow in microfluidic T-junctions, Chem. Eng. Sci. 62 (2007) 7505–7514. https://doi.org/10.1016/j.ces.2007.08.068.

[49] R. Xiong, J.N. Chung, Bubble generation and transport in a microfluidic device with high aspect ratio, Exp. Therm. Fluid Sci. 33 (2009) 1156–1162. https://doi.org/10.1016/j.expthermflusci.2009.07.005.

[50] R. Higbie, The rate of absorption of a pure gas into still liquid during short periods of exposure, Inst. Chem. Eng. 35 (1935) 36–60.

[51] R. Guo, C. Zhu, Y. Yin, T. Fu, Y. Ma, Mass transfer characteristics of CO2 absorption into 2-amino-2-methyl-1-propanol non-aqueous solution in a microchannel, J. Ind. Eng. Chem. 75 (2019) 194–201. https://doi.org/10.1016/j.jiec.2019.03.024.

[52] T. Deleau, J.-J. Letourneau, S. Camy, J. Aubin, F. Espitalier, Determination of mass transfer coefficients in high-pressure CO2-H2O flows in microcapillaries using a colorimetric method, Chem. Eng. Sci. 248 (2022) 117161. https://doi.org/10.1016/j.ces.2021.117161.

[53] N. Dietrich, K. Loubière, M. Jimenez, G. Hébrard, C. Gourdon, A new direct technique for visualizing and measuring gas–liquid mass transfer around bubbles moving in a straight millimetric square channel, Chem. Eng. Sci. 100 (2013) 172–182. https://doi.org/10.1016/j.ces.2013.03.041.

[54] V. Talimi, Y.S. Muzychka, S. Kocabiyik, A review on numerical studies of slug flow hydrodynamics and heat transfer in microtubes and microchannels, Int. J. Multiph. Flow. 39 (2012) 88–104. https://doi.org/10.1016/j.ijmultiphaseflow.2011.10.005.

[55] Z. Pang, S. Jiang, C. Zhu, Y. Ma, T. Fu, Mass transfer of chemical absorption of CO2 in a serpentine minichannel, Chem. Eng. J. 414 (2021) 128791. https://doi.org/10.1016/j.cej.2021.128791.